TIGIT as a therapeutic target of HPV-positive head and neck squamous cell carcinomas

Xiuning Le[1]*, Minghao Dang[2]*, Venkatesh L. Hegde[1], Bo Jiang[1], Ravaen Slay[3], Weihong Xiao[1], Keiko Akagi[1], Joseph Fresquez[1], Kathrina L. Marcelo[1], Qianyun Luo[1], Pragya Sinha[1], Ananta V. Yanamandra[1], Joe Dan Dunn[1], Diana Bell[4], Michelle Williams[4], Edwin Parra[5], Ryan Goepfert[6], Stephen H. Lai[6], Neil Gross[6], Amit Agrawal[7], Alexandre Reuben[1], Jeffrey Myers[6], Michael A. Curran[3], K. Jagannadha Sastry[1], Linghua Wang[2,8#], Maura L. Gillison[1,8#]

[1] Department of Thoracic Head and Neck Medical Oncology
[2] Department of Genomic Medicine
[3] Department of Immunology
[4] Department of Pathology
[5] Department of Translational Molecular Pathology
[6] Department of Head and Neck Surgery
University of Texas MD Anderson Cancer Center
1515 Holcombe Blvd, Houston Texas 77030 USA
[7] Department of Otolaryngology Head and Neck Surgery,
Ohio State University, Columbus, OH 43221
[8] MD Anderson Cancer Center UTHealth Graduate School of Biomedical Sciences, Houston, TX, 77030 USA.
* X.L. and M.D. share first authorship

 # Co-corresponding authors:
Maura Gillison, M.D., Ph.D.
Department of Thoracic Head and Neck Medical Oncology
University of Texas MD Anderson Cancer Center
1515 Holcombe Blvd, Houston Texas 77030 USA
E-mail: mgillison@mdanderson.org
Phone: +1-713-792-6363

Linghua Wang, M.D., Ph.D.
Department of Genomic Medicine, University of Texas MD Anderson Cancer Center,
1881 East Road, Unit 1954, Houston, TX 77054.
E-mail: Lwang22@mdanderson.org
Phone: +1-713-563-2293

Conflict-of-interest statement

X.L. serves consulting, advisory roles for EMD Serono (Merck KGaA), AstraZeneca, Spectrum Pharmaceutics, Eli Lilly, Boehringer Ingelheim, Bristol-Myers Squibb, and Celgene; and receives research funding from Eli Lilly and Boehringer Ingelheim; **M. W.** serves advisory board roles for Roche and Bayer Pharmaceuticals; **S.Y.L.** serves as a medical affairs consultant for Cardinal Health; **N.G.** serves advisory board, consulting roles for Sanofi-Genzyme, Shattuck Labs, PDS Biotechnology, Intuitive Surgical-Consultant; and research funding from Regeneron; **A.R.** serves in the Scientific

Advisory Board and has received honoria from Adaptive Biotechnologies; **M.A.C.** receives grant funding from ImmunoMet Inc.; honoraria/fees for consulting, lectures, speakers bureau, and/or other affiliations (e.g. advisory board) for ImmunoGenesis Inc., Alligator Bioscience Inc., ImmunOS Inc, Oncoresponse Inc., Pieris Inc., Nurix Inc., Aptevo Inc., Servier Inc., Kineta Inc., Salarius Inc., Xencor Inc., Agenus Inc., and Mereo; and patents on methods and composition for localized secretion of anti-CTLA-4 antibodies and anti-PD-L1 and -PD-L2 dual specificity antibodies; **M.L.G.** serves as consulting, advisory board roles for LLX Solutions, LLC (Pending), Sensei, Mirati Therapeutics, BioNTech AG, Shattuck Labs Inc., EMD Serono Inc., Debiopharm, Kura Oncology, Merck Co., Ipsen Biopharmaceuticals Inc., Bristol-Myers Squibb, Bicara Therapeutics, Bayer HealthCare Pharmaceuticals, Roche, Roche Diagnostics GmbH, Genocea Biosciences, Inc., NewLink Genetics Corporation, Aspyrian Therapeutics, TRM Oncology, Amgen Inc.,AstraZeneca Pharmaceuticals, and Celgene Corp.; and research funding from Genocea, BMS, Kura, Cullinan, Genentech, BioNtech, and Gilead. All remaining authors report no conflict.

Abstract

The tumor immune microenvironment (TIME) of treatment-naïve, human papillomavirus-positive head and neck squamous cell carcinoma (HPV-positive HNSCC) was interrogated at single-cell level to identify influential immune checkpoints as therapeutic targets. Single-cell transcriptome profiling revealed enrichment of numerous cell-cell interactions mediated by *TIGIT-PVR/NECTIN2* in the TIME of HPV-positive HNSCC versus normal tonsil. TIGIT was the most differentially upregulated immune checkpoint on clonally expanded $CD8^+$ T cells and was abundant on antigen-experienced, tissue-resident memory $CD8^+$ T cell and T-regulatory subsets. TIGIT ligands *PVR/NECTIN1/2* were abundant on mature regulatory dendritic cells, immunosuppressive plasmacytoid DCs, and macrophages. TIGIT and PD-1 co-blockade in the mEER murine model of HPV-positive HNSCC significantly reduced tumor growth, improved survival, restored effector function of HPV16 E7-specific $CD8^+$ T cells, natural killer cells, and DCs, and conferred tumor re-challenge protection. This immunogenetic analysis at single-cell resolution focusing on HPV-positive HNSCC identified TIGIT as a rational therapeutic target.

Introduction

Human papillomavirus-positive head and neck squamous cell carcinoma (HPV-positive HNSCC) is epidemiologically, genetically, and clinically distinct from HPV-negative HNSCC. HPV-positive HNSCC has an improved prognosis relative to HPV-negative HNSCC (1), hypothesized as due in part to enhanced immune surveillance by greater numbers of tumor-infiltrating lymphocytes (TILs) (2, 3). Nevertheless, approximately 20% of patients with HPV-positive HNSCC experience cancer recurrence (4). Immune checkpoint blockade (ICB) targeting programmed death receptor 1 (PD-1) improves survival relative to platinum-based chemotherapy in patients with recurrent or metastatic HNSCC whose tumors express its ligand, PD-L1 (5). However, response rates are <20% regardless of tumor HPV status, and patients experience cancer progression at a median of ~3 months (6). It is likely that additional immune checkpoints and modulatory molecules in the tumor immune microenvironment (TIME) function to restrict anti-tumor immunity.

An analysis of 280 HPV-negative and HPV-positive HNSCC in which RNA-Seq data were deconvoluted to infer immune cell infiltration revealed that HPV-positive HNSCC is more heavily immune-infiltrated and has a higher median T regulatory cell (Treg) to $CD8^+$ T cell ratio when compared to several other solid tumors, including HPV-negative HNSCC (7). A subsequent analysis of an expanded TCGA dataset (N=500) confirmed higher median expression of CD4 and CD8 mRNA in HPV-positive versus HPV-negative HNSCC, including higher median mRNA expression of the exhaustion markers LAG3, PD-1, TIM3, CD39 and TIGIT (8).

Single-cell RNA sequencing (scRNA-Seq) provides a more nuanced characterization of immune cell populations in the TIME, and thus may guide development of checkpoint inhibitor combinations. Recently, a comparison of $CD45^+$ TILs in HPV-positive HNSCC versus HPV-negative HNSCC with scRNA-Seq revealed distinct $CD4^+$ T cell, B cell, and myeloid cell phenotypic states in the HPV-positive HNSCC versus HPV-negative HNSCC (9), suggesting unique immunomodulatory dependencies. Therefore, immunotherapy combinations may be differentially effective in tumors caused by persistent HPV infection in contrast to chronic carcinogen exposure (e.g., tobacco and alcohol) (10).

Given that HPV-positive HNSCC is distinct from HPV-negative HNSCC, here we intentionally performed single-cell transcriptomic profiling focused exclusively on treatment-naïve, HPV-positive HNSCC to identify inhibitory immune checkpoints highly expressed in the TIME. Our analyses revealed the TIGIT family of immunomodulatory receptors and ligands to be predominant among the cell-cell communication networks in the TIME of HPV-positive HNSCC. Moreover, co-blockade of the TIGIT and PD-1 checkpoints in a mouse model of HPV-positive HNSCC restored effector function of CD8+ T cells (including HPV16 E7-specific CD8+ T cells), natural killer (NK) cells, and antigen-presenting cells (APCs), and enhanced anti-tumor efficacy. Therefore, we nominate TIGIT as a therapeutic target for HPV-positive HNSCC.

Results

Single-cell profiling revealed that TIGIT family molecules were prevalent in HPV-positive HNSCC. To identify dominant immune regulators in the TIME of HPV-positive HNSCC, scRNA-Seq and simultaneous single-cell TCR-Seq were performed on 14 treatment-

naïve HPV-positive HNSCC tumors, and 3 normal tonsils (Supplemental Table 1). After quality filtering and removal of batch effects, we profiled the transcriptome of 72,866 cells, which clustered into subgroups representing nine major cell lineages: tumor and epithelial cells; stromal cells (endothelial, fibroblasts); and 5 major immune cell populations (Figure 1A and Supplemental Figure 1A-1B).

We profiled cell-cell communication networks in the TIME versus normal tonsil using an unbiased approach, iTALK, to characterize ligand-receptor-mediated cellular interactions (11) (Figure 1B; Supplemental Table 2). Among the top 20 most abundant receptor-ligand interactions, *TIGIT-NECTIN2* interactions were recurrent across multiple cell types in tumors (Figure 1B). Gain of interactions between $CD4^+$ and/or $CD8^+$ T cells and tumor cells, DCs, macrophages, or fibroblast cell subsets via enhanced *TIGIT-NECTIN2* signaling was present. The *CTLA4-CD86* axis was also upregulated, whereas interactions mediated by other checkpoint axes (e.g., *CD40LG* and *CD40*, *TNFSF9 [4-1BBL]* and *TNFRSF9 [4-1BB]*, *SEMA4D* and *CD72*) were decreased. These data support *TIGIT-NECTIN2* interactions as influential in modulating anti-tumor immunity in the TIME of HPV-positive HNSCC.

The T Cell Immunoreceptor With Ig and ITIM Domains (TIGIT) family of receptors and ligands (hereafter, receptors/ligands) functions as an immune checkpoint to limit immune responses in model systems of viral infections and cancer (12-14). TIGIT is expressed on T cells and natural killer (NK) cells (15). TIGIT and the related receptor CD96 compete with the co-stimulatory receptor CD226 for binding to ligands Poliovirus Receptor (PVR; CD155), Nectin-2 (CD112) and Nectin-1 (CD111), expressed on APCs and tumor cells (15-18).

When we explored associations between functionally well characterized inhibitory immune checkpoints (19) and overall survival in TCGA bulk RNA-Seq data from patients with HPV-positive HNSCC, the TIGIT axis once again stood out as influential in the TIME (n = 72; Supplemental Table 3). High expression of *PVR* (*CD155*) or *NECTIN2* (*CD112*) most strongly associated with poor overall survival in univariable analysis (Supplemental Figure 2A-2B). In contrast, both *TIGIT* and *PDCD1* (PD-1) expression were associated with favorable survival (Supplemental Figure 2C).These data indicate a strong clinical relevance for the TIGIT-PVR/Nectin-2 axis in HPV-positive HNSCC.

We assessed expression of TIGIT receptors/ligands in several cell types at the single-cell level (Figure 1C). *TIGIT* expression was more frequent in $CD4^+$ and $CD8^+$ T cells than in NK cells, whereas *CD96* was more abundant in $CD8^+$ T cells and NK cells than in $CD4^+$ T cells (Figure 1C). Both *CD226* and *PVRIG* expression were limited to <10% of all cell populations. *PVR* and *NECTIN2* expression varied markedly across tumor, stroma, and myeloid cell populations: both were most highly expressed in endothelial cells and tumor/epithelial cells. In contrast, *NECTIN1* was most highly expressed in tumor/epithelial cells and plasmacytoid dendritic cells (pDCs; Figure 1C). In comparison to PD-1 checkpoint receptor/ligands, TIGIT receptors/ligands were more frequently expressed. *TIGIT* expression was more frequent in T cells overall than *PDCD1* (34.4 % vs. 20.4 % , p=9.1e-292, two-sided proportion test), and *PVR* (12.8%), *NECTIN1* 1 (39.1%), and *NECTIN2* (56.4%) expression were more prevalent on tumor cells than *CD274* (9.3%, for all, p≤3.23e-31, two-sided proportion test)

TIGIT receptors/ligands were enriched in the TIME compared to normal tonsil tissue (Figure 1D). Intra-tumoral CD8$^+$ T cells had significantly higher expression of *TIGIT*, *CD96,* and *CD226*, and CD4$^+$ T cells had higher expression of *TIGIT*. Myeloid cells, fibroblasts, and endothelial cells in the TIME had higher *PVR* and *NECTIN2* expression than in normal tonsil tissue (Figure 1D and Supplemental Figure 1C-1D). *PDCD1* expression by CD8$^+$ T cells was also enriched in the TIME, as was *CD274* (PD-L1) expression by epithelial/tumor cells (Supplemental Figure 1C-1D).

We next quantified RNA expression of TIGIT receptors/ligands and PD1/PD-L1 in individual tumors. Across patients, *TIGIT*, *CD96*, and *PDCD1* expression in tumor-infiltrating CD8$^+$ T cells showed considerable heterogeneity both in frequency and expression level (Figure 1E). Tumor cell expression of *NECTIN2* showed similar heterogeneity, whereas *PVR* and *CD274* expression were overall low across patients (Figure 1E). Although the proportions of CD8$^+$ T cells that expressed *TIGIT, CD96*, and *PDCD1* varied across patients (Figure 1E), within each patient the proportion of CD8$^+$ T cells that expressed *TIGIT* was highly correlated with that of *PDCD1* ($r = 0.56$, $p = 0.04$), *CD96* ($r = 0.67$, $p = 0.011$) and also *CD226* ($r = 0.56$, $p = 0.042$, Figure 1F).

To evaluate protein expression of TIGIT receptors/ligands on the cell surface, we performed flow cytometry on immune cells isolated from HPV-positive HNSCC tumor samples (n=4) in comparison to peripheral blood mononuclear cells (PBMC) from a healthy donor (n=1). The frequency of TIGIT expression on tumor-infiltrating CD8$^+$ and CD4$^+$ T cells appeared higher than healthy PBMC control, whereas CD226 appeared lower (Supplemental Figure 3A-3B). Among tumor-infiltrating myeloid cells, CD112 (Nectin-2) expression appeared more frequent than CD155 (PVR) expression (Supplemental Figure 3C-3D). Frequency of Nectin-2 and PVR expression in tumor-infiltrating myeloids appeared higher than in myeloid cells in PBMC control, across all major myeloid lineages (Supplemental Figure 3C-3D). Similar to our scRNA-Seq results (Figure 1E), the flow cytometry analysis revealed inter-patient variation in TIGIT receptors/ligands expression. Moreover, immunohistochemistry with an experimentally validated PVR antibody (Supplemental Figure 1E) confirmed that PVR expression per scRNA-Seq correlated with PVR cell surface protein expression (Figure 1G). In summary, this analysis of protein expression of TIGIT receptors/ligands was overall consistent with enrichment of these receptor/ligands in the TIME of HPV-positive HNSCC via single-cell mRNA expression. We conclude that TIGIT receptors/ligands are more highly enriched in tumor and tumor-infiltrating immune cells than are PD-1 receptor/ligands and that they predominate among cell-cell communication networks in the TIME of HPV-positive HNSCC.

TIGIT was highly expressed in antigen-experienced, clonally expanded CD8$^+$ T cells. To gain a greater understanding of the phenotype of CD8$^+$ T cells in the TIME of HPV-positive HNSCC, we compared gene expression profiles in CD8$^+$ T cells with and without co-expression of *TIGIT* (Figure 2A and Supplemental Table 4). TIGIT$^+$CD8$^+$ T cells had a marked increase in co-expression of chemokine (C-X-C motif) ligand 13 (*CXCL13*; Supplemental Figure 4A-4B). CXCL13 elicits the formation of tertiary lymphoid structures (20) and was recently linked to neoantigen-specific CD8$^+$ T cells and increased response to PD-1 ICB (21). Additional genes highly co-expressed with *TIGIT* included *ENTPD1* (CD39), an ectonucleotidase that metabolizes ATP to adenosine, and the integrin *ITGAE* (CD103), both markers of tissue-resident memory T

cells (T_{RM} cells). Notably, T_{RM} cells isolated from TILs mediated tumor cell killing *in vitro,* and their frequency was associated with improved survival in HNSCC after adjustment for HPV status (22). Several additional genes significantly co-expressed in TIGIT$^+$CD8$^+$ T cells and indicative of an effector phenotype included *GZMB, HLA-DRA1/DRB1, TNFRSF9* (4-1BB/CD137), and *CTLA4* (Figure 2A). A comparison of gene expression profiles for clonally expanded (clonotype frequency ≥5%) versus non-expanded (<1%) CD8$^+$ T cells identified *TIGIT* as the most differentially upregulated immune checkpoint in expanded CD8$^+$ T cells (Figure 2B and Supplementary Table 4). Overall, these characteristics of TIGIT$^+$CD8$^+$ T cells were consistent with an antigen-experienced, tissue-resident, effector phenotype.

Unsupervised clustering analysis stratified CD8$^+$ T cells into six distinct clusters (Figure 2C-2D and Supplementary Table 5). When compared to normal tonsils, CD8$^+$ T cells in Clusters 1 and 6 were increased significantly in tumors, whereas those in Cluster 5 were significantly reduced (Figure 2E). *TIGIT* expression was significantly more frequent in the CD8$^+$ T cell clusters that were enriched in the TIME (Figure 2G).

Cluster 1 (60.8% TIGIT$^+$) had high expression of *CXCL13, TNFRSF9*(*4-1BB*), *ENDPT1* (*CD39*), granzymes, MHC class II molecules, and several inhibitory checkpoints (e.g., *CTLA4, LAG3,* and *HAVCR2* [*TIM3];* Figure 2C-2D and Supplemental Figure 4B). This cluster also had a high dysfunctional score, a high T_{RM} cell score (Figure 2F), and high TCR clonal expansion (Figure 2H), consistent with an antigen-experienced phenotype. In Cluster 1, ~20% of cells had high expression of *TOX* (Figure 2D and Supplemental Figure 4B), a transcription factor promoting T cell exhaustion (23), but in the context of chronic viral infection, TOX may program progenitor-like CD8$^+$ T cells (24). Cluster 1 contained the CD103$^+$CD8$^+$ T_{RM} cells (Figure 2D and 2F) shown to be strongly associated with improved survival in HPV-positive HNSCC (25).

Cluster 6 (61% TIGIT$^+$) was characterized by high expression of cell proliferative markers (e.g. *MKI67* and *TUBB*) and *TNFRSF18* (*GITR*; Figure 2D), reported to promote proliferation and survival of activated CD8$^+$ T cells and resistance to Treg suppression (26). Analogous to Cluster 1, Cluster 6 cells had high cytotoxicity, dysfunctional and T_{RM} scores (Figure 2F), high TCR clonality (Figure 2H), and high *TOX* expression (Figure 2D), consistent with an antigen-experienced phenotype. Although less frequent, *TIGIT* was moderately expressed on CD8$^+$ T cells in Cluster 2 (34%; Figure 2G) that had a trend toward increased frequency in tumor versus normal tonsils ($p = 0.056$; Figure 2E). This unique cluster was characterized by high expression of *DKK3, GZMK*, and *EOMES* (Figure 2D) and a high naïve-like score (Figure 2F), but nevertheless had a relatively high TCR clonotype frequency (Figure 2H). Overall, CD8$^+$ T cells in Cluster 2 had features of a tolerant phenotype. We conclude that TIGIT was highly expressed in antigen-experienced, TCR-expanded, T_{RM} cell-like, and proliferating CD8$^+$ T cells.

CD96 expression largely mirrored that of *TIGIT*, with enrichment in Clusters 1 (58.2%) and 6 (64.1%; Figure 2D, 2F, and 2I and Supplemental Figure 4C). However, *CD96* was higher in frequency than *TIGIT* in Cluster 4 (50.7% vs 16.6%; Figure 2I), characterized by high expression of *IL7R*, *GNLY*, and the C-type lectin-like receptor *KLRB1* (*CD161*; Supplemental Table S5), and relatively low expression of *CCR7*, *SELL*, *CD27*, and inhibitory checkpoint molecules (Figure 2D). *TNFAIP3 (A20),* an inhibitor of the canonical NF-kB signaling pathway linked to restriction of antitumor activity of CD8$^+$

T cells (27), was also expressed in this cluster (Figure 2D). This phenotype is consistent with an effector memory phenotype important in viral and anti-tumor immunity (28).

TIGIT and *PDCD1* (*PD-1*) were frequently co-expressed in Clusters 1 and 6, whereas co-expression of *CD226* was considerably less frequent (Figure 2I). There was considerable inter-patient variability in the proportion of $CD8^+$ T cells distributed within each cluster in the TIME (Supplemental Figure 4D), with all but Cluster 5 represented in each patient.

TIGIT was frequently expressed and abundant on regulatory T cells (Tregs). Unsupervised clustering separated $CD4^+$ T cells into 6 distinct clusters (Figure 3A-3B and Supplemental Table 5). Analogous to $CD8^+$ T cells, TIGIT was most frequently expressed on the $CD4^+$ T cell clusters present at higher frequency in the TIME versus normal tonsils: Cluster 4, Cluster 5, and Treg (Figure 3A-3D). Cluster 4 had a high frequency of $TIGIT^+$ cells (61.5%; Figure 3C), a trend toward higher frequency in the TIME (Figure 3D), and features of T-follicular helper (Tfh) cells, including high expression of *CXCL13, PDCD1, ICOS, CTLA4,* and *CXCR5* and low expression of *CCR7* (Figure 3A-3B and Supplemental Figure 5A). Notably, a Tfh cell signature was recently found to be associated with improved survival in the TCGA HNSCC database (9). Cluster 5, a proliferative $CD4^+$ T cell cluster, also had a high frequency of $TIGIT^+$ cells (56.3%), some cytotoxic characteristics (Figure 3A-3B), and increased TCR clonality (Supplemental Figure 5B), consistent with an antigen-experienced, Th1-type, $CD4^+$ T cell phenotype.

The highest frequency (68.7%) and abundance of *TIGIT* expression in $CD4^+$ T cells was in the Treg cluster, characterized by high *FOXP3* and *IL2RA* (*CD25*) expression (Figure 3B-3C and Supplemental Figure 5A). Further analysis subclassified Tregs into three subclusters: Treg_C0 had high expression of several activation markers such as *IL2RA (CD25), TNFRSF18 (GITR), TNFRSF4 (OX40);* Treg_C1 had high heat shock protein gene expression (i.e., *HSPA1A, HSPA1B [HSP72]*); and Treg_C2 had naïve markers (*CCR7, SELL*; Figure 3E-3F). When a pseudo-time trajectory was inferred using the naïve-like Treg cells (C2) as the root (Figure 3G), expression of *CTLA4* peaked well into the Treg_C0 activated state, whereas *TIGIT* expression peaked at the naïve-to-active Treg transition as well as at the transition from C0 to C1 state (Figure 3H). Thus, modulation of *TIGIT* could in theory impair the development of suppressive phenotypes in Tregs.

In contrast to $CD8^+$ T cells, patterns of *CD96* expression on $CD4^+$ T cells were distinct from *TIGIT*, with a more diffuse expression pattern across all clusters (Figure 3C and 3I) and highest expression in naïve-like Cluster 3. *PDCD1* (*PD-1*) expression was highest in Cluster 4 (Tfh), and low in Tregs and Cluster 3 (Figure 3B and 3I). There was considerable inter-patient variability in the proportion of $CD4^+$ T cells distributed across clusters (Supplemental Figure 5C). Across patients, *TIGIT* and *PDCD1* expression were positively correlated in $CD4^+$ T cells ($R = 0.58$, $p = 0.032$), whereas *CD96* was not ($R = 0.4$, $p = 0.16$) and *CD226* was inversely correlated, albeit non significantly ($R = -0.042$, $p = 0.89$; Supplemental Figure 5D). In summary, among $CD4^+$ T cells, *TIGIT* was frequently co-expressed with *CTLA4* on Tregs and Tfh cells enriched within the TIME in HPV-positive HNSCC.

NECTIN2 and PVR in the myeloid cells are associated with suppressed TIME. We evaluated the expression of the TIGIT family ligands *PVR*, *NECTIN1, and NECTIN2*

in myeloid populations. Compared to the T cells in the TIME, myeloid cells (n = 3,529) were considerably lower in frequency, and more heterogeneous (Figure 4A and Supplemental Table 5). Neutrophils, a cell population linked to poor prognosis of oropharynx cancer (29), had a higher frequency in the TIME compared to normal tonsil (Figure 4B).

Among the three defined subgroups within the macrophage population, MAC_C1 had a trend toward higher frequency in the TIME (p = 0.056), whereas, MAC_C2 was significantly decreased (p = 0.039; Figure 4B). MAC_C1 had high expression of M2 and angiogenesis gene signatures (Figure 4C-4D), the macrophage-recruiting cytokine *CCL5*, and the M2-polarizing, metastasis-promoting cytokine *CCL18*. Thus, MAC_C1 had a phenotype of tumor-associated macrophages (TAMs; Figure 4C-4D). The Mac_C2 subset had high expression of *HLA-A* and *HLA-C* as well as chemokines (e.g., *CXCL9* and *CXCL10)* that recruit CXCR3-expressing $CD8^+$ T cells associated with response to anti-PD(L)1 (30) (Figure 4C-4D). The Mac_C3 subset highly expressed the T cell co-stimulatory molecules *CD86* and *CCND2*, but had relatively low HLA expression, suggesting an M0 phenotype. All 3 MAC clusters frequently expressed *NECTIN2* (Figure 4E).

Three distinct DC populations were identified: pDC, *LAMP3*$^+$ DC, and cDC1 (Figure 4A). None had differential enrichment between tumor and normal tonsil (Figure 4B), but a trend toward a decrease in the frequency of *LAMP3*$^+$ DCs was observed (p=0.076). The *LAMP3*$^+$ DC population had the highest frequency and abundance of *PVR* and *NECTIN2* expression, as well as high expression of IL-15 (Figure 4C-4E). This $LAMP3^+$ DC cluster had an expression profile consistent with an IFNɣ-exposed, activated and migratory APC (high *IRF1, CD40, CCR7, CCL17,* and *CD80*) (31). Among all the myeloid subsets, this subgroup had the strongest M1-like phenotype, as well as several aspects of a mature regulatory DC GES (Figure 4D), including expression of the Treg recruiting chemokines *CCL22* and the tryptophan metabolizing enzymes IDO1 and KYNU, known to suppress T cell function (32).

The pDC population, marked by high expression of the pDC developmental transcription factors *IRF8* and *TCF4*, expressed an additional member of the nectin family, *NECTIN1 (CD111)*, which has preferential binding to CD96 (33, 34). The pDC population had a highly immunosuppressive gene expression profile, including *VEGFB*, proteases (e.g., *CTSC* [cathepsin C]), and *TGFB1*, as well as high expression of EGFR ligand *AREG*/amphigelulin (Figure 4C and Supplemental Table 5). This is of potential importance given the established role for EGFR signaling in proliferation, metastases, and poor prognosis of HPV-negative HNSCC. Therefore, this pDC population had a tumor-promoting phenotype, perhaps influenced in part by *CD96-NECTIN1* interactions.

Across the 14 patients, the frequency of $TIGIT^+CD8^+$ T cells and $NECTIN2^+$ myeloid cells correlated strongly with IL-6 expression by myeloid cells (R = 0.66, p = 0.013 and R=0.74, p = 0.0035; Figure 4F). Tumor expression of *PVR* was correlated strongly with *NECTIN2* (R = 0.81, p = 0.0007; Figure 4F). Moreover, the frequency of $TIGIT^+$Tregs correlated with the frequency of myeloid cells with an M2 GES. These data align well with the cross-talk we identified in the iTALK analysis (Figure 1B-1D).

In summary, single-cell transcriptomics revealed that *TIGIT* and *CD96* were frequently expressed in tumor-infiltrating $CD8^+$ and $CD4^+$ Tcell subsets enriched within the TIME of HPV-positive HNSCC. *TIGIT* and *CD96* expression were abundant in $CD8^+$

T cells with an antigen-experienced, T_{RM} cell phenotype, and *TIGIT* was frequently co-expressed with *CTLA4* on Tregs. Interactions of these cell populations with *PVR* in LAMP3$^+$DC, *NECTIN1* in pDC, and *NECTIN2* on macrophages and PVR/NECTIN1/NECTIN2 on tumor cells likely contribute to myelosuppressive functions in the TIME.

TIGIT blockade generated anti-tumor immunity and protective memory in a murine model. Given the TIGIT receptors/ligands were highly abundant in HPV-positive HNSCC, we sought to investigate the effect of TIGIT checkpoint modulation on anti-tumor immunity in an *in vivo* immunocompetent mouse model. RNA-Seq data from tumors generated by sublingual injection in syngeneic mice of either lung epithelial (TC-1) (35) or tonsillar epithelial (mEER) (36) cells transformed by HPV16 E6/E7 and H-Ras showed them to have very low versus moderate expression, respectively, of *TIGIT, PVR, NECTIN2* and *PD-L1* (Supplemental Figure 6A). The mEER model was chosen for further analysis due to its more relevant tissue of origin to HPV-positive HNSCC than TC-1.

The mEER cells were inoculated into the base of the tongue of syngeneic mice. Starting on day 5, animals bearing a tumor of ~2 mm in diameter (~5 mm^2) received intraperitoneal injections of either anti-TIGIT antibody every 3 days for 5 doses or an anti-PD1 antibody every 3 days for 3 doses or anti-TIGIT plus anti-PD-1 in combination (Figure 5A). Tumor volume as assessed by MRI imaging on day 19 revealed a significant reduction in all treatment groups when compared to untreated control mice (Figure 5B). Treatment with the combination of anti-TIGIT and anti-PD-1 led to a significantly greater reduction in tumor volume when compared to single-agent therapy (anti-PD-1, -35.1%; anti-TIGIT, -28.5%, anti-TIGIT and anti-PD-1, -73.3%; Figure 5B). Evaluation of H&E stained murine tumors confirmed tumor cell lysis and necrosis with combination treatment (Supplemental Figure 6B). Furthermore, the combination treatment significantly improved survival when compared to single-agent therapy or control (Figure 5C and Supplemental Figure 6C). We conclude that the therapeutic efficacy of TIGIT blockade was similar to that of anti-PD-1 in the mEER model, but anti-TIGIT plus anti-PD-1 combination yielded significantly enhanced benefit.

To identify subsets of immune cells associated with this therapeutic benefit, we performed multiparametric flow cytometry on dissociated cells from tumors resected on day 19 (Figure 5D-5F). No statistically significant changes in the frequencies of infiltrating CD3$^+$, CD4$^+$, or CD8$^+$ T cell subsets were observed in any of the treatment groups when compared to untreated control (Supplemental Figure 6D). However, marked changes were observed in the frequencies of functional subsets of CD8$^+$ T cells. Specifically, the proportion of CD8$^+$ T cells that expressed either GzmB or IFNɣ increased with each single-agent therapy compared to untreated controls. Co-blockade led to a further increase over either single-agent immunotherapy alone. Notably, a 10.8-fold increase (Standard Deviation ±4.8) in dual-functional GzmB$^+$IFNɣ$^+$ CD8$^+$ T cells was observed with anti-TIGIT plus anti-PD-1 relative to controls (One-way ANOVA with Tukey multiple paired comparisons, $p < 0.0001$; Figure 5D).

We sought to determine whether anti-TIGIT and/or anti-PD-1 would modulate tumor antigen-specific immunity by analyzing TILs for HPV16 E7-specific CD8$^+$ T cells using a tetramer reagent corresponding to HPV16 $E7_{49-57}$, an immune dominant epitope (37). Only the combination therapy resulted in a statistically significant increase in

HPV16 E7-specific GzmB$^+$IFNγ$^+$CD8$^+$ T cells: a 4.1-fold (Standard Deviation ±2.6) increase over untreated controls was observed. Similarly, only combination therapy led to a significant increase in the proportion of polyfunctional, activated NK cells (CD3$^-$ NK1.1$^+$ GzmB$^+$IFNγ$^+$; Figure 5E and Supplemental Figure 6D). These data demonstrate a robust induction of multiple cytolytic effector cells, including total and HPV-specific CD8$^+$ T cells in response to co-blockade of TIGIT and PD-1. When the proportion of DCs that had an activated phenotype (CD3$^-$CD11c$^+$, IA/IE$^+$) was examined, only the combination resulted in a significant increase over that of the untreated control group (Figure 5F). None of the treatments significantly altered the frequency of FoxP3$^+$ Tregs (data not shown), consistent with previous reports demonstrating that anti-TIGIT efficacy is not dependent upon Treg depletion (12, 38, 39).

Anti-TIGIT treatment significantly downregulated TIGIT expression on different T cell subsets (CD4$^+$, CD8$^+$ T cells, and Tregs), but not on NK cells (Figure 5G). Importantly, anti-PD-1 alone led to a significant increase in the proportion of CD4$^+$, CD8$^+$, and Tregs that express TIGIT, suggesting TIGIT could mediate acquired resistance to anti-PD-1 therapy. The addition of anti-TIGIT to anti-PD-1 abrogated such an effect (Figure 5G).

Abrogation of CD8$^+$ T cells by use of depleting antibodies prior to co-blockade treatment in mEER tumor-bearing mice led to a significant detriment in survival relative to mice without CD8$^+$ T cell depletion (0/5 survival with depletion vs. 4/5 without depletion, p = 0.0027; Figure 5H and Supplemental Figure 6E). In contrast, NK cell depletion had no significant effect on survival (3/5 vs. 4/5, p = 0.61; Figure 5H and Supplemental Figure 6E). Thus, the anti-tumor effects of co-blockade were highly CD8$^+$ T cell dependent.

To evaluate for immune memory responses, mice that remained tumor-free on day 84 after co-blockade of TIGIT and PD-1 (n = 4) were injected with one million mEER tumor cells on the right flank and monitored for tumor growth. Flank injection was used as a model for distant metastases. A control group of treatment-naïve mice (n = 7) were injected similarly. On day 20 after tumor inoculation, all treatment-naïve mice displayed significant tumor burden (all ≥50 mm^3), whereas the previously treated mice remained tumor-free (Figure 5I). This protection was associated with the presence of HPV16 E7 tetramer$^+$CD62L$^+$CD44^{high} central memory CD8$^+$ T cells prior to tumor cell re-challenge (Figure 5J). These data indicate that co-blockade with TIGIT and PD-1 results in a protective memory response and resistance to tumor re-challenge.

In summary, *in vivo* data from the mEER model of HPV-positive HNSCC demonstrate that co-blockade of the TIGIT and PD-1 checkpoints resulted in restoration of anti-tumor immunity via generation of polyfunctional CD8$^+$ T cells, including HPV16 E7-specific T cells, NK cells, and activated DCs in the TIME. These alterations in the TIME correlated with reductions in tumor volume, delayed tumor growth, increased survival, and generated long-term immune memory to HPV-positive HNSCC.

Discussion

This is the first immunogenetic analysis at single-cell resolution to focus exclusively on HPV-positive HNSCC in order to identify influential immunomodulatory checkpoints in the TIME for rationale selection of immunotherapy combinations. We identified TIGIT receptors/ligands as dominant among immunomodulatory cell-cell communication

networks enriched within the TIME of HPV-positive HNSCC. In our analysis, TIGIT was the most differentially upregulated immune checkpoint on all clonally expanded $CD8^+$ T cells and was abundantly expressed in several $CD8^+$ T cell clusters with an antigen-experienced phenotype enriched within the TIME. The phenotype of $TIGIT^+CD8^+$ T cells in Cluster 1, markedly enriched within the TIME, resembled the $CD103^+$ T_{RM} cells linked to improved survival of HPV-positive HNSCC (25). Given *in vitro* blockade of TIGIT, with or without blockade of PD-1, increased proliferation and functionality of antigen-specific $CD8^+$ TILs isolated from human melanoma and renal cell carcinoma (40, 41), blockade of TIGIT signaling has remarkable potential to restore proliferation and effector function of antigen-experienced $TIGIT^+CD8^+$ T cells enriched in the TIME of HPV-positive HNSCC.

High PVR expression has been associated with poor overall survival in univariable analysis in three independent HNSCC cohorts in which the overwhelming majority of patients had HPV-negative HNSCC (42-44). An analysis of 12 HPV-negative HNSCC by flow cytometry observed higher TIGIT expression on $CD4^+$ and $CD8^+$ TILS compared to peripheral blood, and anti-TIGIT delayed tumor growth in a $CD8^+$ T cell-dependent manner in the murine *Tgfbr1*/*Pten* double knockout model of HPV-negative HNSCC (44). When combined with our data, these data in HPV-negative HNSCC support a potential role for targeting of TIGIT in both distinct cancer subsets.

A significant fraction of $CD8^+$ T cells in HPV-positive HNSCC was characterized by high expression of *DKK3* (Dickkopf-3), *GZMK/M*, and *TGFB1 (Cluster 2)*. Whereas *DKK3* and *TGFB1* have a role in mediating $CD8^+$ T cell tolerance (45), expression of *EOMES, TBX21* (*T-bet*), *CCR7, GZMK/M*, and *TCF7* (*TCF1*) and relatively low levels of inhibitory immune checkpoint genes suggest a central memory phenotype. The high expression of CD28 in this population with relatively low levels of CD27 suggests these are effector memory cells with significant recall potential (46). Given HPV-positive HNSCC occurs as a consequence of tolerance to chronic viral infection, Cluster 2 is of particular clinical interest, as re-activation of Cluster 2 may result in generation of robust anti-tumor responses.

TIGIT expression in $CD8^+$ T cells was variable across patients but highly correlated with PD-1, CD96, and CD226. TIGIT was co-expressed frequently with CD96 and PD-1 on $CD8^+$ T cell clusters with a TCR expanded, antigen-experienced phenotype. These observations may explain in part the enhanced clinical benefit from TIGIT blockade reported in patients with PD-L1 positive non-small cell lung cancer in recent clinical trials (47, 48). In contrast, co-expression of TIGIT with CD226 was infrequent, particularly on $CD4^+$ T cells. Given frequent co-expression of CD96 and TIGIT on $CD8^+$ T cells, as well as high CD96 expression on NK cells, triple-blockade of CD96, TIGIT and PD-1 may further enhance effector function. Preclinical models in other cancer types have shown that anti-CD96 augments $CD8^+$ T cell function and anti-tumor immunity imparted by co-blockade of TIGIT and PD-1 (49) and enhanced NK cell antitumor activity in $TIGIT^{-/-}$ mice (50). A weakness in our study was insufficient NK cell numbers for clustering analysis.

$TIGIT^+CD4^+$ T cells had increased expression of *FOXP3, CTLA4, IL2RA, BATF*, and *CD27*, consistent with activated, immunosuppressive Tregs. $TIGIT^+$ Treg frequency correlated with the proportion of myeloid cells with an M2 gene expression signature, supporting immunosuppressive cross-talk between Tregs and myeloid cells via the

TIGIT-PVR/NECTIN2 axis. TIGIT$^+$CD8$^+$ T cell frequency also correlated with the proportion of myeloid cells producing IL-6, suggesting additional cross-talk among CD8$^+$ T cells and myeloid cells within the TIME. PD-L1, PVR, and Nectin-2 were co-expressed on the LAMP3$^+$ DC population, with gene expression signature indicative of highly potent APCs (51). The increase in activated APCs we observed in the mEER model could be due to indirect benefits from enhanced pro-inflammatory conditioning by T cells or NK cells freed from TIGIT suppression and/or as a result of removal of pro-suppressive "back-signaling" from engaged TIGIT ligands (15, 52). Activation of LAMP3$^+$DCs with co-blockade of TIGIT and PD-1 may promote CD8$^+$ T cell anti-tumor immunity, APC function, and facilitate neoantigen spreading.

HPV-positive cancers develop in part due to CD8$^+$ T cell exhaustion and/or tolerance to viral proteins. Perhaps our most important observation is that co-blockade of TIGIT and PD-1 increased HPV16 E7-specific GzmB$^+$INFγ$^+$ CD8$^+$ T cells in the mEER model. The mEER syngenic, immunocompetent model was chosen for analysis because the tumors are of tonsillar epithelial origin transformed by HPV16 E6, E7, and HRAS and are injected into the oral tongue to model oropharynx cancer. In this model, the TIGIT and PD-1 ICP combination generated a population of HPV16 E7-specific central memory CD8$^+$ T cells that conferred protection upon tumor rechallenge. These data directly implicate TIGIT in the suppression of HPV-specific immunity.

HPV-positive HNSCC is established as distinct from HPV-negative HNSCC, so extrapolation of data from models of HPV-negative HNSCC to positive HNSCC should be avoided. In our *in vivo* mEER model of HPV-positive HNSCC, the single-agent activity of anti-TIGIT was similar to that of anti-PD-1. Similar single-agent activity was reported in the *Tgfbr1*/*Pten* knockout model of HPV-negative HNSCC (44), demonstrating the potential importance of TIGIT immunoregulation in both HPV-positive HNSCC and HPV-negative HNSCC. Unique to our analysis, co-blockade of TIGIT and PD-1 further improved efficacy, attributable to enhanced effector function of CD8$^+$ T cells, NK cells, and DCs. Depletion studies confirmed a strong dependence on CD8$^+$ T cells, as reported previously in the *Tgfbr1*/*Pten* knockout model of HPV-negative HNSCC (44). An increased frequency of activated, polyfunctional GzmB$^+$IFNγ$^+$ NK cells also contributed to the anti-tumor activity. Our observation of increased frequency of activated DCs aligns well with recent data that FcγR engagement on APCs is important for the anti-tumor efficacy of TIGIT blockade in mouse models (38, 39). In contrast to the *Tgfbr1*/*Pten* double knockout model of HPV-negative HNSCC, we did not observe a reduction in intratumoral Treg frequency in the mEER model with the anti-TIGIT BE0274 IgG1 isotype antibody (Bio X Cell). Perhaps the mEER HPV-positive HNSCC model has a higher frequency or abundance of TIGIT on Tregs than the *Tgfbr1*/*Pten* double knockout model of HPV-negative HNSCC. Intratumoral Treg depletion has been reported with several anti-TIGIT antibodies (e.g., the CT26 colon model) (41, 53, 54), due to higher Fc affinity for FcγR and stronger induction of ADCC.

In the mEER model, we provided direct evidence of TIGIT upregulation upon PD-1 blockade, and co-blockade of TIGIT and PD-1 abrogated this effect. We observed the frequency of TIGIT expression on CD8$^+$ T cells, CD4$^+$ T cells, and Tregs increased significantly in the mEER model after anti-PD-1 alone, in agreement with *in vitro* studies on antigen-specific CD8$^+$ T cells among TILS isolated from melanoma patients (40). Moreover, TIGIT expression was increased in resected, nonresponding HNSCC tumors

after neoadjuvant PD-1 (55). Collectively, these data indicate TIGIT may mediate primary and/or adaptive resistance to anti-PD-1. Given that both TIGIT and PD-1 have an immunoreceptor tyrosine-based inhibition motif (ITIM) to negatively regulate T cell anti-tumor responses, TIGIT upregulation after blockade of PD-1 suggests a functional redundancy for tumors to escape immune attack through either PVR and/or PD-L1/L2 expression. It is worth noting that in the mEER model, the CTLA4 and PD-1 ICB combination also induced an increase in E7-specific $CD8^+$ T cell mediated killing (56), consistent with our data that the CTLA4/CD86 axis is also enriched in the TIME of HPV-positive HNSCC. Future investigation of the PD-1, TIGIT, CTLA4 ICB combination in the mEER model is therefore warranted.

In summary, our data indicate that the TIGIT immunoregulatory network of receptors and ligands is markedly enriched in the TIME of HPV-positive HNSCC. We demonstrate that co-blockade of TIGIT and PD-1 restored effector function of HPV-specific $CD8^+$ T cells, NK, and DCs in the mEER model, leading to improved response, survival, and generation of protective memory. Our data support rapid clinical development of co-blockade of TIGIT and PD-(L)1 in patients with HPV-positive HNSCC and inform phamacodynamic endpoints of interest to be evaluated in human subjects.

Methods

Patient populations. Fresh tumor was collected at the time of diagnostic biopsy or surgical resection from 14 treatment-naïve patients with HPV-positive HNSCC. Normal tonsil tissue was obtained from three of these patients. Detailed patient information is presented in Supplemental Table 1. Three additional treatment-naïve tumor samples were processed for flow cytometry analysis.

Single-cell RNA sequencing and TCR sequencing on the 10X platform. Fresh tumors were evaluated by clinical pathology to confirm tumor versus normal, placed in 10% FBS RPMI 1640 media, and transferred to the laboratory for immediate processing. Tissue was dissociated per single-cell suspension protocol (Supplemental Methods). Fresh single-cell suspensions were used for generation of transcriptome and TCR profiling libraries per 10xGenomics 5'RNAseq (Chromium Single Cell 5' Library and Gel Bead Kit v1) and TCRseq (Chromium Single Cell V[D]J Reagent Kits [v1 Chemistry] and V[D]J Enrichment Kit) protocols. Library quality was assessed using high sensitivity capillary electrophoresis on a Fragment Analyzer (TapeStation: High Sensitivity 5000 from Agilent Technologies). Libraries were pooled at ration 1:10 (TCR: GEX) and sequenced at NovaSeq 6000 Sequencing System (Illumina) at 150 x 150 bp with a minimum of 5,000 read pairs per cell for V(D)J Enriched library and a minimum of 20,000 read pairs per cell for 5' Gene Expression library.

Analysis of Single-Cell RNA-Seq data. The raw scRNA-seq data were pre-processed (demultiplex cellular barcodes, read alignment to human reference genome build, and generation of gene count matrix) using Cell Ranger Single Cell Software Suite (v3.1.0) provided by 10x Genomics. Detailed QC metrics were generated and evaluated. Cells with low complexity libraries or likely cellular debris (in which detected transcripts are aligned to less than 200 genes) were filtered out and excluded from subsequent analyses. Low-quality cells where >15% of transcripts derived from the mitochondria genome were considered apoptotic and also excluded. In addition, cells with detected genes >6,000 were discarded to remove likely doublet or multiplet

captures. The resulting cells were clustered and further filtered using a multi-step approach to clean additional possible doublets (Supplemental Methods). Tumor and stromal and non-T/NK immune cells with productive TCRs were removed. In addition, we carefully reviewed canonical marker gene expression in defined cell clusters and further cleaned out cells/clusters expressing discrepant lineage-specific markers. The above steps were repeated multiple times to ensure the elimination of most barcodes associated with cell doublets. Following the removal of poor-quality cells and doublets, a total of 72,866 cells were retained for downstream analysis. Library size normalization was performed using the function *NormalizeData* in Seurat v3 (version 3.1.1) (57) on the filtered gene-cell matrix to obtain the normalized UMI count.

Seurat v3 (version 3.1.1) (57) was applied to the normalized gene-cell matrix to identify highly variable genes (HVGs) for unsupervised cell clustering. Principal component analysis (PCA) was performed on the top 2000 HVGs. The elbow plot was generated with the *ElbowPlot* function of Seurat and based on which, the number of significant principal components (PCs) were determined. Harmony (58) was used to remove batch effects in the PCA space with the default parameters. The *FindNeighbors* function of Seurat was used to construct the Shared Nearest Neighbor (SNN) Graph, based on unsupervised clustering performed with Seurat function *FindClusters*. Different resolution parameters for unsupervised clustering were then examined in order to determine the optimal number of clusters. For visualization, the dimensionality was further reduced using Uniform Manifold Approximation and Projection (UMAP) method (59) with Seurat function *RunUMAP*. The PCs used to calculate the embedding were the same as those used for clustering.

Two rounds of clustering (clustering and subclustering) were performed to identify major cell types (CD4 T cells, CD8 T cells, NK cells, B cells, plasma cells, myeloid cells, fibroblast cells, endothelial cells, and epithelial cells) and cell transcriptomic states within $CD4^+$ T cells, $CD8^+$ T cells and myeloid cells. In both rounds, 30-nearest neighbors of each cell were determined based on 30 PCs to construct SNN graphs. Differentially expressed genes (DEGs) were identified for each cluster using the *FindAllMarkers* function in Seurat R package. Top-ranked DEGs in each cell cluster were carefully reviewed and cell clusters were annotated according to the enrichment of canonical marker genes. Malignant cells were identified based on an integrative approach including the expression of tumor cell-specific HPV genes, the CNV profiles inferred from single-cell RNA sequencing data using inferCNV (v1.5.0) [https://github.com/broadinstitute/inferCNV], as well as cluster distribution and oncogene expression features.

Ligand-Receptor interaction analysis. To identify significant ligand-receptor (L-R) pairs, we first defined the highly expressed genes in each cell type, using an approach similar to that of Zhang et al (60), as the genes with an expression level log2(normalized UMI+1)>0.5 in at least 20% of the cells of that type. Then we matched these highly expressed genes with the curated list of L-R pairs from iTALK(11) to identify the potentially interacting ligand-receptor pairs. We assume two cell types within a sample have interaction when one highly expressed ligand/receptor and the other one highly expressed the paired receptor/ligand. For the differential interactome analysis, we first identified the differentially expressed genes in each cell type between tumors and normals using the function *FindMarkers* from Seurat v3 (version 3.1.1) (57) with

parameter min.pct = 0.2 and then matched these DEGs with the iTALK L-R database. We defined increased interactions if the expression of a ligand or receptor was upregulated while its paired receptor or ligand was not downregulated. We also scored each interaction using the same way as herein described (60) and showed the top-ranked interactions in the circus plot.

TCR V(D)J sequence assembly, paired clonotype calling, and integration with scRNA-seq data. Cell Ranger v3.1.1 for V(D)J sequence assembly was applied for TCR reconstruction and paired TCR clonotype calling. The CDR3 motif was located and the productivity was determined for each cell. The clonotype landscape was then assessed and the clonal fraction of each identified clonotype was calculated. The TCR clonotype data was then integrated with the T cell phenotype data inferred from single-cell gene expression analysis based on the shared unique cell barcodes.

Signature scores of CD8$^+$ T cells and myeloid cells. Dysfunctional score, naïve like score, and cytotoxic score were calculated for each CD8 T cell using the ssgsea method in GSVA software package. Dysfunctional gene signature includes *HAVCR2*, *GZMB*, *IFNG*, *CXCL13*, *PDCD1*, *ITGAE*, *LAYN*, *LAG3*, *TIGIT*, *CTLA4*, *ENTPD1*, naïve like gene signature includes *TCF7*, *CCR7*, *SELL*, *LEF1*, *IL7R*, *LTB,* and cytotoxic gene signature includes *CX3CR1*, *PRF1*, *GZMA*, *GZMB*, *GZMH*, *GNLY*, *FGFBP2*, *KLRG1*, *FCGR3A*, *GZMK*, *LYAR*, *GZMM*, *TXNIP*, *FCRL6*, *NKG7*, *KLRD1*, as summarized by van der Leun et al (61). Similarly, the expression of M1, M2, angiogenesis, and phagocytosis features were calculated for each myeloid cell using defined gene signatures (51).

Trajectory analysis. Monocle3 (version 0.2.0; http://cole-trapnell-lab.github.io/monocle-release/monocle3/) (62) was applied to construct the single-cell trajectories of Tregs. The raw gene-cell count matrix was normalized and preprocessed using *preprocess_cds*. Potential batch effect was corrected using function *align_cds*. The dimensionality reduction was performed on the 'Aligned' matrix using function *reduce_dimension* with default parameters. The function *cluster_cells* and *plot_cells* were used for unsupervised clustering and visualization of the Monocle clustering results. The function *learn_graph* was run with default parameters to build the trajectory. For the pseudotime analysis, we selected the naïve-like cluster as the root of the trajectory.

Immunohistochemistry for PVR. Cell pellets from 293T cells transfected with a PVR expression vector or empty vector control were evaluated by Western blot for PVR expression and then fixed in formalin buffer, pre-embedded in agarose, and paraffin-embedded. FFPE cell pellets cut in 4µm thick sections mounted on positively charged slides were deparaffinized and retrieved in Citrate Buffer, pH 6.0. Slides were incubated at 4°C overnight with primary antibody PVR (Abcam, Cambridge MA), followed by peroxidase blocking. EnVision Dual Link System-HRP (DAB; Dako, Agilent, Santa Clara, CA) was used for signal development. The slides were mounted in paramount after hematoxylin counterstaining. Images were taken in Zeiss Axio Observer 7 Motorized Inverted Microscope (Zeiss, Oberkochen, Germany). After validation, the procedure was performed on FFPE from patients in the single-cell analysis cohort.

Flow cytometry of human immune cells. Peripheral blood mononuclear cells (PBMC)s were enriched from one healthy donor whole-blood sample using a Ficoll gradient (Histopaque-1077, Sigma-Aldrich) as previously described (63). Treatment-

naïve HPV-positive HNSCC biopsies (n=4) were dispersed into single cell suspensions, and then total immune cells were enriched through density gradient separation over Histopaque 1119 (Sigma-Aldrich) as previously described (64). The PBMCs and tumor immune cells were fixed and permeabilized overnight in Foxp3/Transcription Factor Fixation/Permeabilization solution (ThermoFisher Scientific), washed in FACs buffer (PBS + 2% human AB serum + penicillin/streptomycin/gentamicin), and resuspended in blocking buffer and Human TruStain FcX (1:100; Biolegend) for 15 minutes. After blocking, cells were incubated in antibody cocktail (Supplemental Methods) for 2 hours at 4°C, washed in FACS buffer, and then filtered through a 70-μm filter. Flow data were collected on a BD LSRFortessa flow cytometer (BD Biosciences) and analyzed using FlowJo version 10.

Analysis and immune checkpoint modulation in the HPV16-positive mEER syngeneic murine model. Male C57BL/6 mice (5–10 weeks) were purchased from the Jackson Laboratories and maintained per MDACC protocol. Mice were implanted with $4x10^4$ mEER cells in 50 μl PBS into the base of the tongue to allow tumor formation. Mice were monitored closely and euthanized when a necrotic tumor was observed and/or when the mice lost 20% or more of their initial weight. The following antibodies for *in vivo* administration were purchased from Bio X Cell (West Lebanon, NH) and used at the concentrations shown: α-PD-1 (RMP1–14 at 25 mg/kg per mouse intraperitoneal for 5 doses) and α-TIGIT (1G9 from Bio X Cell, 25 mg/kg per mouse intraperitoneal for 5 doses).

Mice exhibiting long-term survival from clearing the oral mEER tumors from the anti-TIGIT and anti-PD-1 combination therapy were subjected to tumor re-challenged by subcutaneous injection of 1 million fresh mEER tumor cells on the right flank on day 84. Naïve mice injected similarly with mEER tumor cells served as the control group. Tumor growth was monitored over 40 days. Two days prior to re-challenge antigen-specific CD8 T cell memory response was assessed in the blood by flow cytometry to detect E7 tetramer$^+$ CD62L$^+$CD44^{high} central memory (CM) population.

For characterization of TIL, mice were euthanized at the days specified in the results section. Tongue tumors were collected and digested per dissociation protocol (65). Percoll gradient purified leukocytes were stained for multi-parametric flow cytometry analysis with 16-color antibody panels (Supplemental Methods). Cells were blocked with mouse Fc-block, stained with surface markers, fixed and permeabilized with the Fix/Perm Kit (eBioscience, Waltham, MA) followed by staining for intracellular markers. Samples were run in an LSR-II X-20 Fortessa (BD Biosciences, San Jose, CA) at the South Campus Flow Cytometry Core, MD Anderson Cancer Center (Houston, TX) and analyzed using FlowJo version 10 (Flowjo LLC, Ashland, OR). The live/dead fixable aqua dye (Thermo Scientific, Waltham, MA) was used to gate out dead cells and to include only live cells for analysis. Live leukocyte gate was set based on forward and side scatter to include both lymphocytes and larger myeloid cells. HPV E7+ tumor antigen-specific CD8 T cells were identified by surface staining using APC-conjugated H-2Db/HPV16-E7 Tetramer synthesized by Baylor College of Medicine MHC tetramer facility (Houston, TX). Tregs were identified based on CD4+Foxp3+ expression within the CD3+ gate. To determine the TIGIT expression, PerCP-eFluor 710 rat anti-Mouse TIGIT (Clone: GIGD7) antibody (ThermoFisher Sci, Waltham, USA) was used to evaluate the mean fluorescence intensity on each cell populations. Anti-CD8 ablation

antibody (Clone: 2.43) and anti-NK1.1 ablation antibody (Clone: PK136) were purchased from Bio X Cell.

Statistical analyses. In addition to the algorithms described above, all other basic statistical analysis was performed in the R statistical environment (v4.0.0). All statistical tests performed in this study were two-sided. Statistical significance of differences observed between tumor and normal was determined by non-parametric Wilcoxon rank-sum test when comparing continuous variables like gene expression level (Figures 1D/1F, 2G, 3F, and 4D). The Spearman's correlation coefficient was calculated to assess the association between two continuous variables (such as expression levels of two genes, proportions of two cell types) at sample level. To control the false discovery rate (FDR) and correct p-values for multiple testing, we apply the Benjamini-Hochberg method(66)and an FDR adjusted p-value (or q-value) < 0.05 is considered as statistically significant.

All differences and statistics in the mouse model experiments were calculated using GraphPad Prism version 8. Statistical significance was determined using one-way or two-way ANOVA along with Tukey's multiple comparison tests to detect differences between the two groups. Mantel-Cox log-rank test was used to compare survival curves. P values less than 0.0332 were considered significant.

Study approval. Patient samples for scRNA-Seq and flow cytometry were obtained under MD Anderson Cancer Center research protocols LAB02-039, PA18-0782, PA19-0470. All three protocols were approved by MDACC institutional review board with active status. Each patient was given information on the study, and the risks and benefits were discussed. All participating patients gave their informed consent. The mouse experiments were conducted under protocol 00000858-RN03, approved by the MDACC institutional animal care and use committee.

Author Contributions

Conceptualization, X.L., K.J.S., L.W. and M.L.G.; Experimental Conduction and Methodology, M.D., V.L.H., B.J., R.S., W.X., K.A., J.F., K.L.M., Q.L., P.S., A.Y., D.B., M.W., E.P., R.G., S.L., N.G., A.A.; Formal Analysis, X.L., M.D., V.L.H., E.P., A.R., M.C., K.J.S., L.W., M.L.G.; Resources, K.J.S., L.W. and M.L.G; Writing – Original Draft, X.L., M.D., L.W., M.L.G.; Writing – Review & Editing, X.L., M.D., J.D.D., A.R., K.J.S., L.W. and M.L.G.; Supervision, L.W. and M.L.G. X.L. contributed to conception, method development, sample acquisition, data interpretation, writing, review and editing. M.D. contributed to the entire bioinformatics analysis of single-cell transcriptomics, data interpretation, review and editing. Therefore, they share first authorship with X.L being the first listed.

Acknowledgments

We thank Drs. Mehmet Altan, Faye Johnson, Charles Lu, Carol Lewis for their contribution of patient samples, Drs. Ruiping Wang and Guangchun Han for their assistance with single-cell data analysis, and Dr. Nils-Petter Rudqvist for his intellectual discussion and editing of the manuscript. Dr. Xiuning Le is supported by Stiefel Oropharyngeal Research Fund and ASCO Conquer Cancer Foundation. Dr. Linghua Wang is supported by start-up funds kindly provided by The University of Texas MD Anderson Cancer Center. This research was supported by the Oral Cancer Foundation,

CPRIT, the Ohio State University, The University of Texas MD Anderson Cancer Center HPV-related Cancers Moonshot, and NCI Grant CA016672(ATGC) for The University of Texas MD Anderson Cancer Center Advanced Technology Genomics Core. Dr. Gillison is a CPRIT Scholar in Cancer Research.

References

1. Gillison ML, et al. Evidence for a causal association between human papillomavirus and a subset of head and neck cancers. *J Natl Cancer Inst.* 2000;92(9):709-20.
2. Ward MJ, et al. Tumour-infiltrating lymphocytes predict for outcome in HPV-positive oropharyngeal cancer. *Br J Cancer.* 2014;110(2):489-500.
3. Wang J, et al. HPV-positive status associated with inflamed immune microenvironment and improved response to anti-PD-1 therapy in head and neck squamous cell carcinoma. *Sci Rep.* 2019;9(1):13404.
4. Ang KK, et al. Human papillomavirus and survival of patients with oropharyngeal cancer. *N Engl J Med.* 2010;363(1):24-35.
5. Burtness B, et al. Pembrolizumab alone or with chemotherapy versus cetuximab with chemotherapy for recurrent or metastatic squamous cell carcinoma of the head and neck (KEYNOTE-048): a randomised, open-label, phase 3 study. *Lancet.* 2019;394(10212):1915-28.
6. Le X, et al. Evolving Role of Immunotherapy in Recurrent Metastatic Head and Neck Cancer. *J Natl Compr Canc Netw.* 2020;18(7):899-906.
7. Mandal R, et al. The head and neck cancer immune landscape and its immunotherapeutic implications. *JCI Insight.* 2016;1(17):e89829.
8. Gameiro SF, et al. Treatment-naive HPV+ head and neck cancers display a T-cell-inflamed phenotype distinct from their HPV- counterparts that has implications for immunotherapy. *Oncoimmunology.* 2018;7(10):e1498439.
9. Cillo AR, et al. Immune Landscape of Viral- and Carcinogen-Driven Head and Neck Cancer. *Immunity.* 2020;52(1):183-99 e9.
10. Shewale JB, et al. Independent association of marijuana use and poor oral hygiene with HPV-negative but not HPV-positive head and neck squamous cell carcinomas. *Cancer.* 2021;127(12):2099-110.
11. Wang Y, et al. iTALK: an R Package to Characterize and Illustrate Intercellular Communication. *bioRxiv.* 2019.
12. Johnston RJ, et al. The immunoreceptor TIGIT regulates antitumor and antiviral CD8(+) T cell effector function. *Cancer Cell.* 2014;26(6):923-37.
13. Zhang Q, et al. Blockade of the checkpoint receptor TIGIT prevents NK cell exhaustion and elicits potent anti-tumor immunity. *Nat Immunol.* 2018;19(7):723-32.
14. Johnston RJ, et al. Cancer Immunotherapy and the Nectin Family. *Annual Review of Cancer Biology.* 2021;5(1):203-19.
15. Yu X, et al. The surface protein TIGIT suppresses T cell activation by promoting the generation of mature immunoregulatory dendritic cells. *Nat Immunol.* 2009;10(1):48-57.
16. Lozano E, et al. The TIGIT/CD226 axis regulates human T cell function. *J Immunol.* 2012;188(8):3869-75.

17. Li XY, et al. CD155 loss enhances tumor suppression via combined host and tumor-intrinsic mechanisms. *J Clin Invest.* 2018;128(6):2613-25.
18. Chan CJ, et al. The receptors CD96 and CD226 oppose each other in the regulation of natural killer cell functions. *Nat Immunol.* 2014;15(5):431-8.
19. Rumpret M, et al. Functional categories of immune inhibitory receptors. *Nat Rev Immunol.* 2020;20(12):771-80.
20. Kazanietz MG, et al. CXCL13 and Its Receptor CXCR5 in Cancer: Inflammation, Immune Response, and Beyond. *Front Endocrinol (Lausanne).* 2019;10:471.
21. Litchfield K, et al. Meta-analysis of tumor- and T cell-intrinsic mechanisms of sensitization to checkpoint inhibition. *Cell.* 2021;184(3):596-614 e14.
22. Duhen T, et al. Co-expression of CD39 and CD103 identifies tumor-reactive CD8 T cells in human solid tumors. *Nat Commun.* 2018;9(1):2724.
23. Khan O, et al. TOX transcriptionally and epigenetically programs CD8(+) T cell exhaustion. *Nature.* 2019;571(7764):211-8.
24. Yao C, et al. Single-cell RNA-seq reveals TOX as a key regulator of CD8(+) T cell persistence in chronic infection. *Nat Immunol.* 2019;20(7):890-901.
25. Solomon B, et al. Identification of an excellent prognosis subset of human papillomavirus-associated oropharyngeal cancer patients by quantification of intratumoral CD103+ immune cell abundance. *Ann Oncol.* 2019;30(10):1638-46.
26. Ward-Kavanagh LK, et al. The TNF Receptor Superfamily in Co-stimulating and Co-inhibitory Responses. *Immunity.* 2016;44(5):1005-19.
27. Giordano M, et al. The tumor necrosis factor alpha-induced protein 3 (TNFAIP3, A20) imposes a brake on antitumor activity of CD8 T cells. *Proc Natl Acad Sci U S A.* 2014;111(30):11115-20.
28. Konduri V, et al. CD8(+)CD161(+) T-Cells: Cytotoxic Memory Cells With High Therapeutic Potential. *Front Immunol.* 2020;11:613204.
29. Takenaka Y, et al. Prognostic role of neutrophil-to-lymphocyte ratio in head and neck cancer: A meta-analysis. *Head Neck.* 2018;40(3):647-55.
30. House IG, et al. Macrophage-Derived CXCL9 and CXCL10 Are Required for Antitumor Immune Responses Following Immune Checkpoint Blockade. *Clin Cancer Res.* 2020;26(2):487-504.
31. Alferink J, et al. Compartmentalized production of CCL17 in vivo: strong inducibility in peripheral dendritic cells contrasts selective absence from the spleen. *J Exp Med.* 2003;197(5):585-99.
32. Fallarino F, et al. The combined effects of tryptophan starvation and tryptophan catabolites down-regulate T cell receptor zeta-chain and induce a regulatory phenotype in naive T cells. *J Immunol.* 2006;176(11):6752-61.
33. Holmes VM, et al. Interaction between nectin-1 and the human natural killer cell receptor CD96. *PLoS One.* 2019;14(2):e0212443.
34. Seth S, et al. The murine pan T cell marker CD96 is an adhesion receptor for CD155 and nectin-1. *Biochem Biophys Res Commun.* 2007;364(4):959-65.
35. Lin KY, et al. Treatment of established tumors with a novel vaccine that enhances major histocompatibility class II presentation of tumor antigen. *Cancer Res.* 1996;56(1):21-6.

36. Hoover AC, et al. The role of human papillomavirus 16 E6 in anchorage-independent and invasive growth of mouse tonsil epithelium. *Arch Otolaryngol Head Neck Surg.* 2007;133(5):495-502.
37. Feltkamp MC, et al. Vaccination with cytotoxic T lymphocyte epitope-containing peptide protects against a tumor induced by human papillomavirus type 16-transformed cells. *Eur J Immunol.* 1993;23(9):2242-9.
38. Han JH, et al. Effective Anti-tumor Response by TIGIT Blockade Associated With FcgammaR Engagement and Myeloid Cell Activation. *Front Immunol.* 2020;11:573405.
39. Waight JD, et al. Selective FcgammaR Co-engagement on APCs Modulates the Activity of Therapeutic Antibodies Targeting T Cell Antigens. *Cancer Cell.* 2018;33(6):1033-47 e5.
40. Chauvin JM, et al. TIGIT and PD-1 impair tumor antigen-specific CD8(+) T cells in melanoma patients. *J Clin Invest.* 2015;125(5):2046-58.
41. Preillon J, et al. Restoration of T-cell Effector Function, Depletion of Tregs, and Direct Killing of Tumor Cells: The Multiple Mechanisms of Action of a-TIGIT Antagonist Antibodies. *Mol Cancer Ther.* 2021;20(1):121-31.
42. Lim SM, et al. Overexpression of poliovirus receptor is associated with poor prognosis in head and neck squamous cell carcinoma patients. *J Cancer Res Clin Oncol.* 2021.
43. Yao Y, et al. Prognostic value of novel immune-related genomic biomarkers identified in head and neck squamous cell carcinoma. *J Immunother Cancer.* 2020;8(2).
44. Wu L, et al. Blockade of TIGIT/CD155 Signaling Reverses T-cell Exhaustion and Enhances Antitumor Capability in Head and Neck Squamous Cell Carcinoma. *Cancer Immunol Res.* 2019;7(10):1700-13.
45. Papatriantafyllou M, et al. Dickkopf-3, an immune modulator in peripheral CD8 T-cell tolerance. *Proc Natl Acad Sci U S A.* 2012;109(5):1631-6.
46. Romero P, et al. Four functionally distinct populations of human effector-memory CD8+ T lymphocytes. *J Immunol.* 2007;178(7):4112-9.
47. Rodriguez-Abreu D, et al. Primary analysis of a randomized, double-blind, phase II study of the anti-TIGIT antibody tiragolumab (tira) plus atezolizumab (atezo) versus placebo plus atezo as first-line (1L) treatment in patients with PD-L1-selected NSCLC (CITYSCAPE). *Journal of Clinical Oncology.* 2020;38(15_suppl):9503-.
48. Niu J, et al. 1410P Safety and efficacy of vibostolimab, an anti-TIGIT antibody, plus pembrolizumab in patients with anti-PD-1/PD-L1-naive NSCLC. *Annals of Oncology.* 2020;31:S891-S2.
49. Mittal D, et al. CD96 Is an Immune Checkpoint That Regulates CD8(+) T-cell Antitumor Function. *Cancer Immunol Res.* 2019;7(4):559-71.
50. Blake SJ, et al. Suppression of Metastases Using a New Lymphocyte Checkpoint Target for Cancer Immunotherapy. *Cancer Discov.* 2016;6(4):446-59.
51. Cheng S, et al. A pan-cancer single-cell transcriptional atlas of tumor infiltrating myeloid cells. *Cell.* 2021;184(3):792-809 e23.

52. Vitale M, et al. NK-dependent DC maturation is mediated by TNFalpha and IFNgamma released upon engagement of the NKp30 triggering receptor. *Blood.* 2005;106(2):566-71.
53. Yang F, et al. A Cross-Species Reactive TIGIT-Blocking Antibody Fc Dependently Confers Potent Antitumor Effects. *J Immunol.* 2020;205(8):2156-68.
54. Chen F, et al. TIGIT enhances CD4(+) regulatory T-cell response and mediates immune suppression in a murine ovarian cancer model. *Cancer Med.* 2020;9(10):3584-91.
55. Uppaluri R, et al. Neoadjuvant and Adjuvant Pembrolizumab in Resectable Locally Advanced, Human Papillomavirus-Unrelated Head and Neck Cancer: A Multicenter, Phase II Trial. *Clin Cancer Res.* 2020;26(19):5140-52.
56. Dorta-Estremera S, et al. Targeting interferon signaling and CTLA-4 enhance the therapeutic efficacy of anti-PD-1 immunotherapy in preclinical model of HPV(+) oral cancer. *J Immunother Cancer.* 2019;7(1):252.
57. Butler A, et al. Integrating single-cell transcriptomic data across different conditions, technologies, and species. *Nat Biotechnol.* 2018;36(5):411-20.
58. Korsunsky I, et al. Fast, sensitive and accurate integration of single-cell data with Harmony. *Nat Methods.* 2019;16(12):1289-96.
59. Becht E, et al. Dimensionality reduction for visualizing single-cell data using UMAP. *Nat Biotechnol.* 2018.
60. Zhang L, et al. Single-Cell Analyses Inform Mechanisms of Myeloid-Targeted Therapies in Colon Cancer. *Cell.* 2020;181(2):442-59 e29.
61. van der Leun AM, et al. CD8(+) T cell states in human cancer: insights from single-cell analysis. *Nat Rev Cancer.* 2020;20(4):218-32.
62. Cao J, et al. The single-cell transcriptional landscape of mammalian organogenesis. *Nature.* 2019;566(7745):496-502.
63. Hegde A, et al. A Phase I Dose-Escalation Study to Evaluate the Safety and Tolerability of Evofosfamide in Combination with Ipilimumab in Advanced Solid Malignancies. *Clinical Cancer Research.* 2021;27(11):3050-60.
64. Jayaprakash P, et al. Targeted hypoxia reduction restores T cell infiltration and sensitizes prostate cancer to immunotherapy. *The Journal of Clinical Investigation.* 2018;128(11):5137-49.
65. Dorta-Estremera S, et al. Mucosal HPV E6/E7 Peptide Vaccination in Combination with Immune Checkpoint Modulation Induces Regression of HPV(+) Oral Cancers. *Cancer Res.* 2018;78(18):5327-39.
66. Benjamini Y, et al. Controlling the false discovery rate in behavior genetics research. *Behav Brain Res.* 2001;125(1-2):279-84.

Figure 1

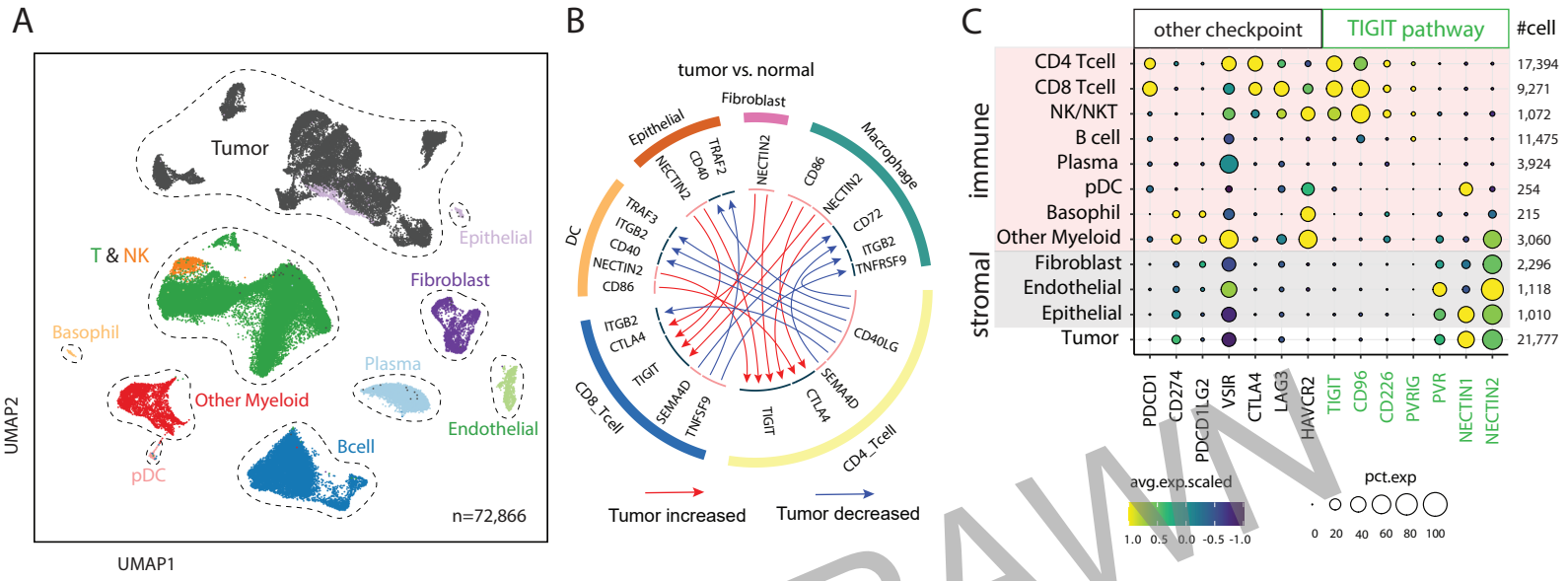

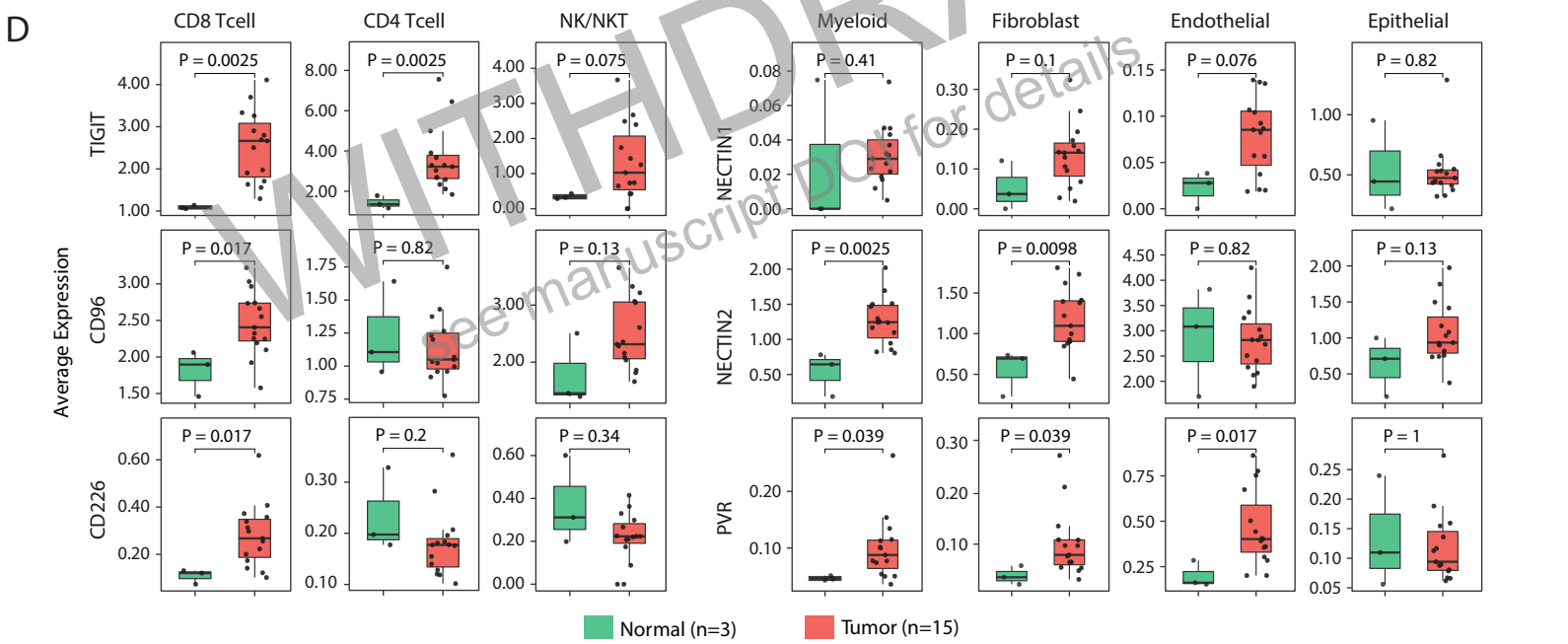

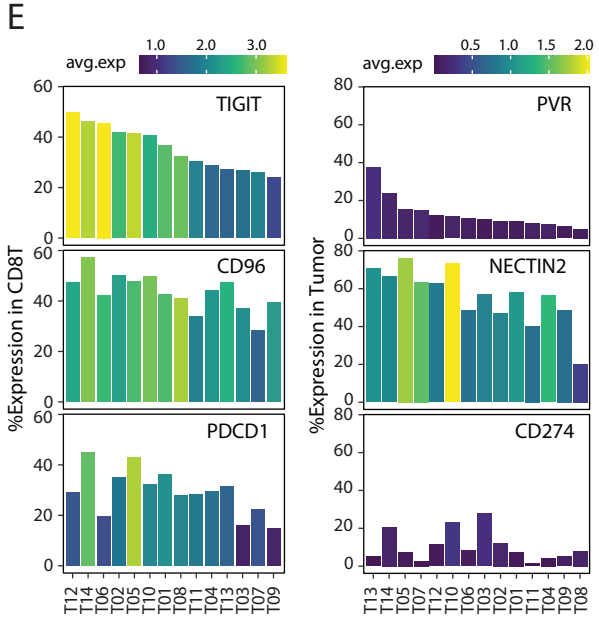

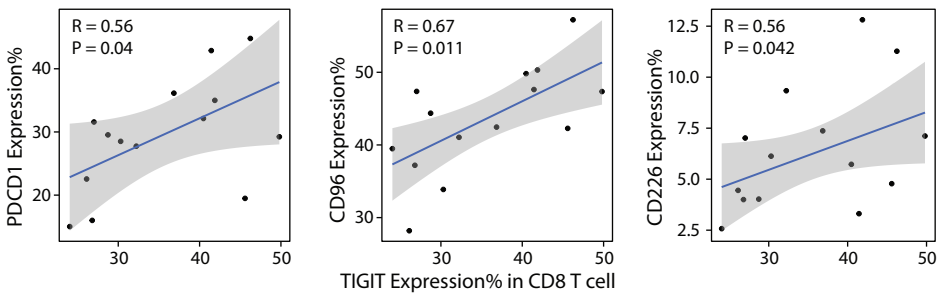

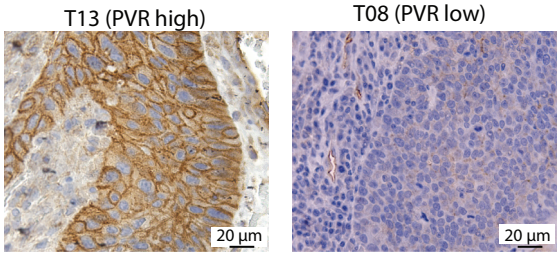

Figure 1. TIGIT family receptors/ligands were abundantly expressed in HPV-positive HNSCC. (**A**) Uniform manifold approximation and projection (UMAP) visualization of unsupervised clustering of all cells (n = 72,866) that passed quality filtering. (**B**) Circos plot of comparative Ligand-Receptor immune checkpoint interactions per iTALK in cell types indicated in tumor versus normal tonsil. Interactions enhanced (*red arrows*) and reduced (*blue arrows*) in tumors versus normal are shown. (**C**) Bubble plot, mean (*color key, top right*) and percent expression (*size key, bottom right*) in cell types indicated (*left*) of *TIGIT* family receptor/ligands and canonical immune checkpoint genes. (**D**) Comparison in tumor versus normal tonsil of the expression levels for *TIGIT, CD96, CD226* in $CD4^+$ T cells, $CD8^+$ T cells, or NK cells (*right*) and *NECTIN1, NECTIN2, PVR* in myeloid, fibroblast, endothelial, epithelial cells (*left*) . Box, median ± interquartile range. Whiskers, range. P values *(<0.05, bold*), two-sided Wilcoxon rank-sum test. (**E**) Bar plots, mean expression (*color key*) and percent (*bar height*) in each tumor of (*left*) $CD8^+$ T cells expressing *TIGIT, CD96,* or *PDCD1* and (*right*) tumor cells expressing *PVR, NECTIN2,* or *CD274*, as measured by scRNA-Seq (N = 14). (**F**) Spearman correlation between the percent of $CD8^+$ T cells with *TIGIT* expression and percent of $CD8^+$ T cells *with PDCD1(Left), CD96 (middle), and CD226* (*right*). Each dot represents a single patient. Shaded area, 95^{th} confidence interval. (**G**) PVR immunohistochemistry of indicated tumors, see also (**E**).

Figure 2. *TIGIT* was highly expressed in antigen-experienced, clonally expanded CD8⁺ T cells. Volcano plots of differentially expressed genes between (**A**) *TIGIT*⁺CD8⁺ T cells and *TIGIT*⁻CD8⁺ T cells and (**B**) CD8⁺ T cells with TCR clonotype frequency ≥5% (Expanded) vs. <1%. (Not-expanded). FDR, two-sided Wilcoxon rank sum test with Bonferonni correction. Dashed line, logFC > 0.3 or < -0.3. Labels, biologically important genes. (**C**) Uniform manifold approximation and projection (UMAP) visualization of unsupervised subclustering analysis of CD8⁺ T cells (n = 9,271). Labelled, representatively enriched genes in each cluster. (**D**) Bubble plot, mean (*color key, bottom right*) and frequency (*size key, bottom left*) of expression of select genes (*X-axis*) in CD8⁺ T cells overall (*bottom row*) and clusters (*y-axis*), grouped by biological functions (*top*). (**E**) Comparison of the proportion of CD8⁺ T cells in clusters indicated (*top*) in tumor (red) versus normal (green) tonsil. Box, median ± interquartile range. Whiskers, range. P values calculated by a two-sided Wilcoxon rank-sum test. (**F**) UMAP as per **c** with cells colored by dysfunctional score, naïve-like score, cytotoxic score (*top, left to right*), and T_{RM} score (*bottom left*) calculated using ssGSEA method, or colored by Log((normalized UMI count)+1) expression of *TIGIT* and *CD96* (*bottom, middle and right*). Proportion of cells with expression indicated. (**G**) Alluvial plot, frequency of *TIGIT*⁺ and *TIGIT*⁻ cells in each cluster. Yellow, significant enrichment in *TIGIT*⁺ cells. Blue, significant enrichment in *TIGIT*⁻ cells. P-values, hypergeometric test for each cluster (* P<0.05, ** P<0.01, *** P<0.001). (**H**) Stacked bar chart, TCR clonal expansions at clonotype frequency indicated (*key*) in CD8⁺ T cell clusters (left) and *TIGIT*⁺ and TIGIT⁻ CD8⁺ T cells. (**I**) Stacked bar chart, % of cells (*y-axis*) with co-expression of *TIGIT* and *PDCD1 (left), CD96 (middle), or CD226* (*right*) in each CD8⁺ T cell cluster (*x-axis*). Clusters ordered by frequency of *TIGIT expression.*

Figure 3

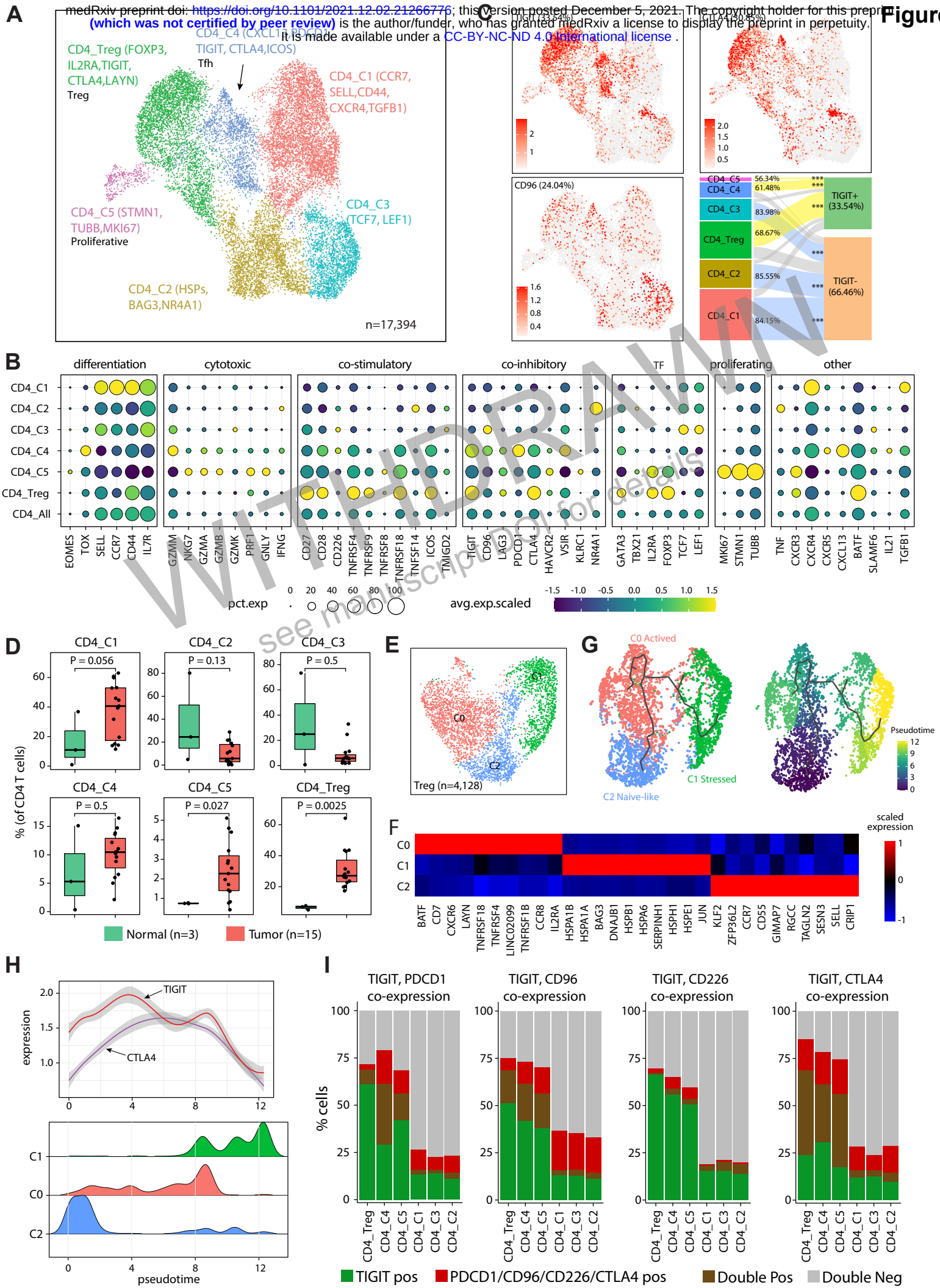

Figure 3. *TIGIT* was highly enriched in T regulatory cells (Tregs). (**A**) Uniform manifold approximation and projection (UMAP) visualization of unsupervised clustering analysis of $CD4^+$ T cells (n = 17,394). Labelled, representatively enriched genes in each cluster. (**B**) Bubble plot, mean (*color key, bottom right*), and frequency (*size key, bottom left*) of expression of select genes (*X-axis*) in $CD4^+$ T cell overall (*bottom row*) and clusters (*y-axis*), grouped by biological functions (*top*). (**C**) UMAP as in (**A**) superposed by expression levels (*color key, bottom left*) and percent of expression (*top left in parentheses*) of *TIGIT, CTLA4*, and *CD96* in $CD4^+$ T cells. Alluvial plot (*bottom right*), proportion (left end of the bands) and significance of enrichment (right end of the bands) of *TIGIT* positive and *TIGIT* negative cells in each CD4 T cells subsets. Yellow bands, significant enrichment of *TIGIT* positive cells. Blue bands, significant enrichment of *TIGIT* negative cells. * P<0.05, ** P<0.01, *** P<0.001, hypergeometric test. (**D**) Comparisons of proportion of $CD4^+$ T cell in clusters indicated (*top*) in tumor (*red*) versus normal tonsil (*green*). Box, median ± interquartile range. Whiskers, range. P values were calculated by a two-sided Wilcoxon rank-sum test. (**E**) UMAP visualization of unsupervised sub-clustering analysis of Tregs (n=4,168). (**F**) Heatmap, scaled expression of top 10 DEGs of each Treg sub-cluster. (**G**) UMAP visualization of Tregs from Monocle3 with inferred trajectory, cluster label (*left*) and pseudo-time (*right*) mapped as per key (*bottom, right*). (**H**) Two-dimensional plots showing the dynamic changes in expression levels of *TIGIT* and *CTLA4* along the pseudotime (*top panel*). Shaded band, 95th confidence interval. Density plot showing the distribution of Treg sub-clusters during the transition along with the pseudotime (*bottom panel*). (**I**) Stacked bar chart, % of cells (*y-axis*) with co-expression of *TIGIT* and *PDCD1, CD96, CD226, CTLA4* in each $CD4^+$ T cell cluster (*x-axis*).

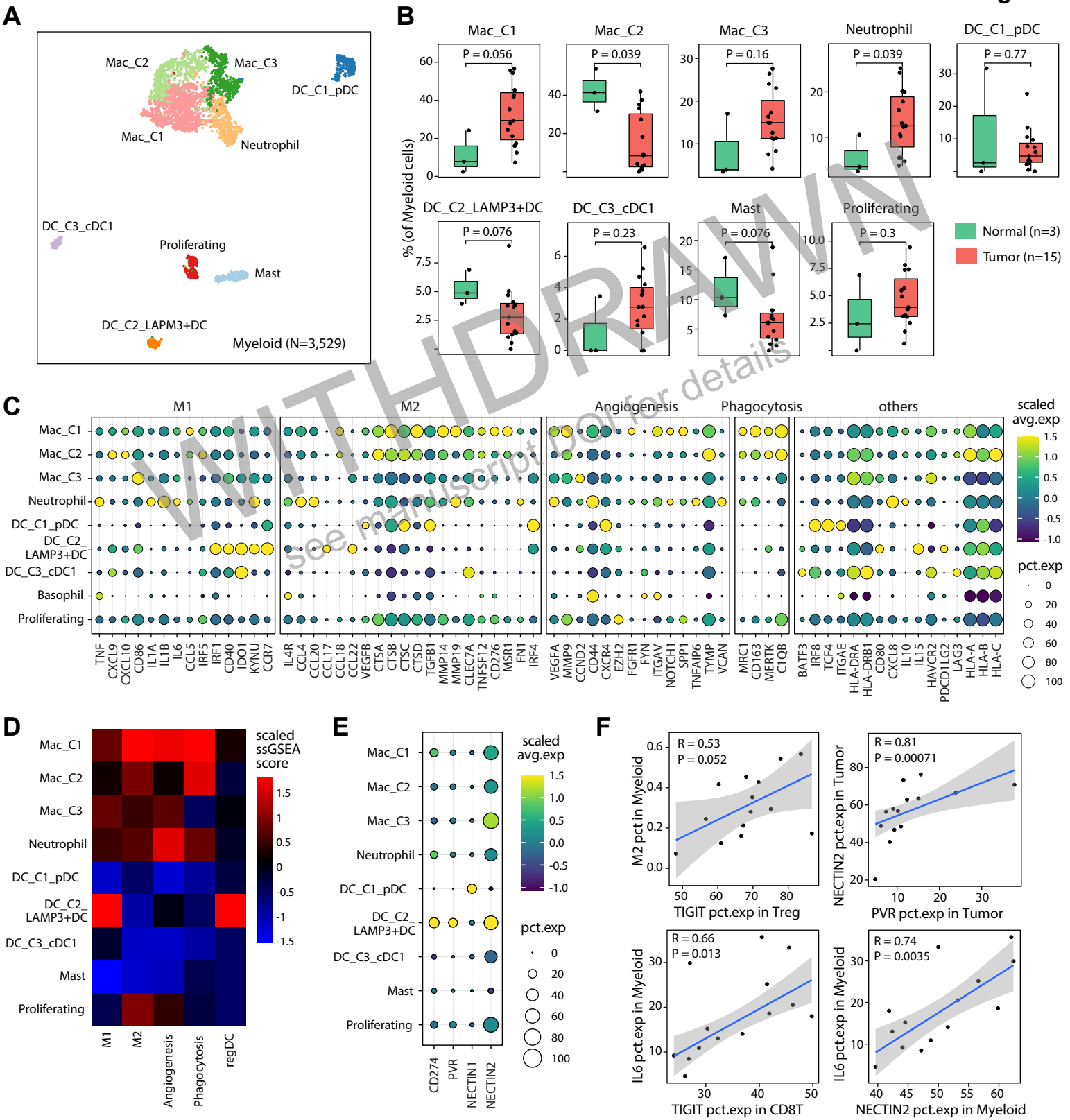

Figure 4. *NECTIN2* and *PVR* in the myeloid cells were associated with suppressed TIME. (**A**) Uniform manifold approximation and projection (UMAP) visualization of unsupervised subclustering analysis of myeloid cells (n = 3,529). (**B**) Comparison of the proportion of the myeloid clusters indicated (*top*) between tumor (*red*) and normal tonsil (*green*). Box plot, median ± interquartile range. Whiskers, range. P values *(<0.05, bold*) were calculated by a two-sided Wilcoxon rank-sum test. (**C**) Bubble plot, mean (*key, top right*) and frequency of expression (*key, bottom right*) of expression of select genes across different myeloid clusters. Genes grouped by biological function (*top*). (**D**) Heatmap, scaled M1, M2, Angiogenesis, Phagocytosis, and mature regulatory DC calculated using ssGEA method in each myeloid cluster. (**E**) Bubble plot, mean (*color key, top right*) and frequency of expression (*size key, bottom right*) of *PD-L1*, *PVR*, *NECTIN1*, *NECTIN2* (*x-axis*) across different myeloid clusters (*y-axis*). (**F**) Spearman correlation between % of indicated cell population that expressed TIGIT (*left, top and bottom panel*) or NECTIN2 (right, bottom panel) and % of all myeloid cells that express IL-6 or an M2 GES. Top right panel, spearman correlation between % of tumor cells that express PVR vs. Nectin 2. Each dot represents a primary tumor sample. Shaded band, 95th confidence interval.

Figure 5

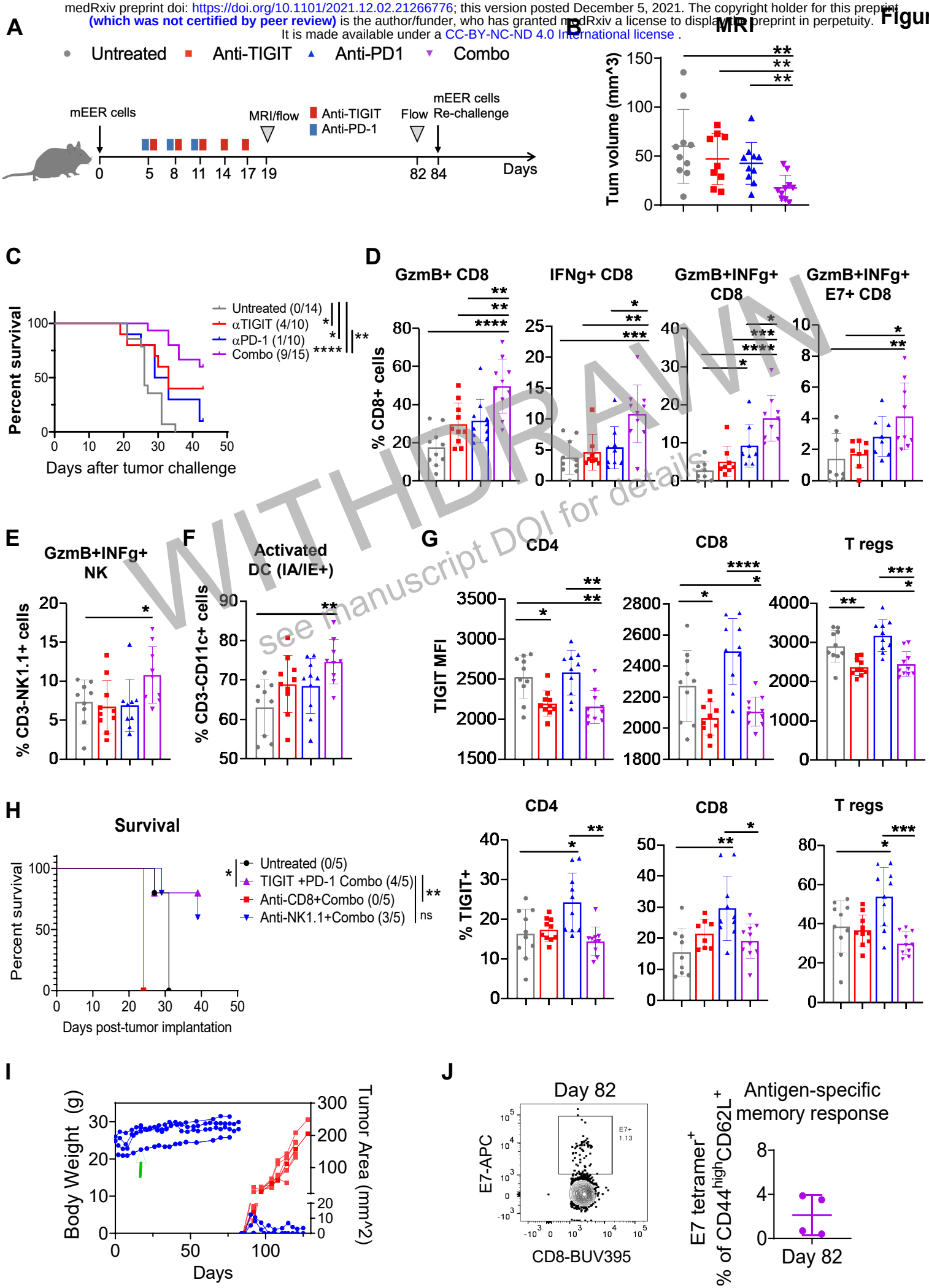

Figure 5. TIGIT blockade with and without PD-1 blockade in the mEER murine model. (**A**) Schema of drug treatment and analysis timepoints in the mEER tumor mouse model experiments. C57BL/6 mice inoculated in the base of the tongue with mEER tumor cells were treated with anti-TIGIT, anti-PD1, or combination at indicated time points. Tumor re-challenge with an injection of 1 million mEER cells in the flank occurred on day 84. Untreated mice served as controls. (**B**) Comparison of tumor size measured by MRI on day 19 between groups using *t*-test (n=10 mice per group and representative of two independent eperiments). **p<0.0021. (**C**) Survival of mice in each treatment group, compared by Mantel-Cox test (n=10-15 mice per group from two separate experiments). *p <0.0332, ****p < 0.0001. (**D**-**G**) Mean ± standard deviation, p-values for one-way ANOVA with Tukey multiple paired comparisons post-hoc test (n= 10 mice per group and representative of two independent experiments). *p <0.0332, **p < 0.0021, ***p < 0.0002, ****p < 0.0001. (**D**) Frequency of $CD8^+$ T cells that express INFɣ, granzyme B (GzmB) or both (*from left to right*). Frequency of HPV16 $E7_{49-57}$ antigen-specific $CD8^+$ T cells that co-express GzmB and INFɣ in TIL as measured by tetramer staining by flow cytometry on day 19 (*far right*). (**E**) Frequency of NK cells that co-express $GzmB^+$ and $INF\gamma^+$. (**F**) Frequency of activated dendritic cells (IA/IE+). (**G**) Mean fluorescence intensity (MFI) of TIGIT cell surface expression was in CD4, CD8, and Treg populations (*top panel*). Frequency of $TIGIT^+$ cells in CD4, CD8 and Treg populations (*bottom panel*). (**H**) Survival of mEER oral tumor-bearing mice treated with anti-CD8 or anti-NK1.1 twice weekly from one day prior to first treatment, compared by Mantel-Cox test (n=5 mice per group). Mice in combo groups were treated with 3 doses of anti-PD1 and 5 doses of anti-TIGIT as shown in (**A**). *p <0.0332, **p < 0.0021. (**I**) Tumor size (mm^2) and animal weight in mice with tumor re-challenge. Tumor-free mice after anti-TIGIT and anti-PD1 combination treatment (*blue*) and treatment-naïve control mice (*red*) were injected in the right flank with one million mEER tumor cells on day 84 and monitored for tumor growth (n=4-5 mice per group). Green arrow, time of last immunotherapy (day 17). (**J**) Detection of HPV16 $E7_{49-57}$ antigen-specific $tetramer^+$ $CD62L^+CD44^{high}$ central memory (CM) $CD8^+$ T cell population by flow cytometry on day 82 before tumor re-challenge. Representative dot plot (left) and aggregate data for 4 mice (*left*).